J Mater Sci (2019) 54:4340–4353

Metals

Microstructural origins of martensite stabilization in $Ni_{49}Co_1Mn_{37.5}Sn_{6.5}In_6$ metamagnetic shape memory alloy

P. Czaja[1,*], J. Przewoźnik[2], M. Kowalczyk[3], A. Wierzbicka-Miernik[1], J. Morgiel[1], and W. Maziarz[1]

[1] The Aleksander Krupkowski Institute of Metallurgy and Materials Science, Polish Academy of Sciences, 25 Reymonta St, 30-059 Kraków, Poland

[2] Department of Solid State Physics, Faculty of Physics and Applied Computer Science, AGH University of Science and Technology, Al. Mickiewicza 30, 30-059 Kraków, Poland

[3] Faculty of Materials Science and Engineering, Warsaw University of Technology, 141 Wołoska St., 02-507 Warsaw, Poland

Received: 7 July 2018
Accepted: 7 November 2018
Published online: 14 November 2018

ABSTRACT

Ordering effects in the $Ni_{49}Co_1Mn_{37.5}Sn_{6.5}In_6$ alloy were studied by subjecting the alloy to annealing at 1220 K followed by water quenching and to subsequent annealing at 1070 K followed by slow cooling. Martensitic transformation temperature increases by 10 K owing to the slow cooling process, which further invites a change in the martensite structure: 6M → 10M. Across the transformation, regardless of the heat treatment applied, austenite phase is paramagnetic and it transforms into a weakly magnetic martensite. Magnetic moment of martensite is boosted due to slow cooling ($\Delta\mu_{\mathrm{eff}}^{\mathrm{M}} = 1\mu_{\mathrm{B}}$). Observed behaviours are associated with the changes in the degree of atomic ordering. Irrespective of the magnetic state of martensite, ordering process mitigates the transformation temperature most likely through the interaction with the free energy difference and through the influence of antiphase domains on the twinning stress.

Introduction

High-temperature quenching coupled with post-quench annealing heat treatment has proved effective for control of the normalized temperature difference between the martensitic transformation (MT) temperature (T_{MT}) and the Curie temperature of austenite phase ($T_{\mathrm{C}}^{\mathrm{A}}$); i.e. $\delta^{\Delta T} = \left(T_{\mathrm{C}}^{\mathrm{A}} - T_{\mathrm{MT}}\right)/T_{\mathrm{C}}^{\mathrm{A}}$, in Ni–Mn base metamagnetic shape memory alloys (MSMAs). While such thermal treatments are found useful for tuning various functionalities of MSMA, their mode of action appears to descend from the sensitivity of MSMA to a varying degree of quenched-in disorder (B2) [1–3]. For instance in Ni–Mn–In alloy, where the $T_{\mathrm{C}}^{\mathrm{A}} \gg T_{\mathrm{MT}}$, the increase in the quenching temperature brings about a decrease in the $\delta^{\Delta T}$, due to a counter-evolution of $T_{\mathrm{C}}^{\mathrm{A}}$ and T_{MT} promoted by a disruption in the ordered $L2_1$ state [4]. In more general, the B2–$L2_1$ transformation in Ni–Mn–In system is experimentally elaborated at

Address correspondence to E-mail: p.czaja@imim.pl

https://doi.org/10.1007/s10853-018-3112-8

$T_{ord.} \sim 965$ K, and neutron diffraction measurements confirmed a progressive collapse of the order parameter as the temperature nears the B2/$L2_1$ transition [4]. Thus, quenching from around or above the $T_{ord.}$ permits partial retention of in-equilibrium disorder, quantified according to the B2/$L2_1$ ratio, which can be qualitatively inferred for a given alloy from the evolution of intensities of the superlattice reflection peaks, such as (111) and (311), relative to the ordered alloy [3, 4]. Following quenching, the development of both T_C^A and T_{MT} in, e.g., Ni–Mn–In system can be reversed by application of a lower temperature ($< T_{ord.}$) secondary annealing step. The $\delta^{\Delta T}$ is then successfully recovered along with a slight boost in saturation magnetization of the austenite phase (M_{sat}^A), provided that the secondary annealing is allowed sufficient length of time and temperature (diffusion) to promote atomic reordering. Interestingly, the other archetypical metamagnetic system, i.e. Ni–Mn–Sn [5], appears to be exempt from this behaviour [6]. The Ni–Mn–Sn system has been found immune to the effect of high-temperature quenching showing only marginal influence of solution heat treatments (SHTs) on the next-nearest-neighbour atomic ordering. This extraordinary resilience to solutionizing has been ascribed in this instance to the unusual stability of the $L2_1$ structure in Ni–Mn–Sn, which holds up until close to the melting point (1300 K) [6]. The practical implications are that neither the $\delta^{\Delta T}$ nor the M_{sat}^A can be effectively adjusted in Ni–Mn–Sn alloys through the conservation of the B2/$L2_1$ ratio.

Thermodynamically, the susceptibility of the $\delta^{\Delta T}$ to SHT derives from the magnetic contribution to the free energy difference across the MT. In simple terms, the increase of order encourages ferromagnetic exchange coupling, noting the atomic distance-dependent magnetization (M) in MSMA [7], and hence stabilizes the more ferromagnetic phase [8]. For a classical MSMA ($\Delta M < 0$ on forward MT), this implies: T_{MT} (↓), whereas T_C^A (↑), e.g. in the above-mentioned Ni–Mn–In [4]. Therefore, when the MT is saddled across two paramagnetic phases, SHT should, in principle, yield null effect on the T_{MT} in MSMA [8]. The mutual impact between the magnetic and atomic orders in response to SHT can be more quantitatively evaluated when considering the MT entropy change (ΔS_{MT}) dependence on the $\delta^{\Delta T}$. The ΔS_{MT} (↓) is found to decrease with increasing $\delta^{\Delta T}$(↑) for a number of MSMA. A more recently developed phenomenological model based on the Bragg–Williams approximation provides the premise for understanding of the causes for ΔS_{MT} change with $\delta^{\Delta T}$ [9]. The model accounts primarily for the vibrational ($\Delta S_{MT}^{vib.}$) and magnetic ($\Delta S_{MT}^{mag.}$) inputs into the overall ΔS_{MT}; i.e. $\Delta S_{MT} = \Delta S_{MT}^{vib.} + \Delta S_{MT}^{mag.}$ [9]. Accordingly, upon the transformation the ΔS_{MT} will receive a magnetic contribution, whose magnitude and sign depend on the magnetic states of the transforming phases. For a model MSMA system, i.e. ferromagnetic austenite transforming into a weakly magnetic/paramagnetic martensite, the ΔS_{MT} becomes: $\Delta S_{MT}^{ferro\rightarrow para} = \Delta S_{MT}^{vib.} < 0 + \Delta S_{MT}^{mag.} > 0$ [9]. In this sense, owing to the magnetic contribution and uneven distance (hysteresis) between the martensite start (M_s) and austenite start (A_s) temperatures to T_C^A, the ΔS_{MT} on the forward ($\Delta S_{MT}^{A\rightarrow M}$) and reverse ($\Delta S_{MT}^{M\rightarrow A}$) MT may differ in absolute values. For illustration, in the above example of ferromagnetic austenite → paramagnetic martensite, the MT would yield $\left|\Delta S_{MT}^{A\rightarrow M}\right| < \left|\Delta S_{MT}^{M\rightarrow A}\right|$ [10]. The inequality in ΔS_{MT} does not violate the second law of thermodynamics but rather is a reflection of the amount of a magnetic phase taking part in the transformation, and since it may be easily accessed through, e.g., calorimetric measurements, it offers a handy and first glance insight into the transformation characteristics. Other peculiar effects, including kinetic arrest phenomenon, have too been recognized in relation to magnetic contribution to ΔS_{MT} [11, 12].

Regarding the magnetic states of the transforming phases, the more classical scenarios of (1) ferromagnetic → weak magnetic/paramagnetic, (2) paramagnetic → paramagnetic and (3) ferromagnetic → ferromagnetic transformations have already been well discussed in the literature together with predicted evolution of ΔS_{MT} [13]. Nonetheless, some controversy still remains in particular in relation to frustrated magnetic states of martensite, which are frequently unveiled in MSMA [14–16], and also in reference to intermittent ferromagnetism of austenite, meaning $M_f \leq T_C^A \leq M_s$ (M_f—martensite finish) or $T_C^A \leq M_f$, and their role in shaping the ΔS_{MT}. More recent results have, for instance, demonstrated contradictory behaviour of, e.g., $Ni_{48}Mn_{39.5}Sn_{9.5}Al_3$ [17] and $Ni_{45}Co_5Mn_{36.6}In_{13.4}$ [18, 19] MSMA for which, irrespective of the magnetic contribution, annealing

process advances the M_s to higher temperatures in spite of a clear enhancement in the degree of order. Simultaneously, the magnetic response of martensite appears altered in the wake of the thermal treatment [15–18, 20, 21]. Clearing these issues is worthwhile, given the widespread applicability of SHT to the control of, e.g., martensite structure [15, 17] and of the overall functional performance of MSMA [22]. Thus, the present paper provides a thorough evaluation of the microstructure and magnetic properties in solutionized and slow-cooled $Ni_{49}Co_1Mn_{37.5}Sn_{6.5}In_6$ MSMA and discusses their bearing on the $\delta^{\Delta T}$ and ΔS_{MT}. The T_{MT} is found to increase with increasing degree of order, what is likely ascribable to the microstructural influence of antiphase boundaries on martensite stability.

Experimental details

The composition of the studied alloy was devised based on Ni, Mn, In and Sn content. The Co was introduced at small amount (1 at.%) in order to enhance ferromagnetism ($T_C^A \uparrow$, $T_{MT}\downarrow$) [3, 23]. Hence, the initial master ingot with the nominal composition of $Ni_{49}Co_1Mn_{37.5}Sn_{6.5}In_6$ was elaborated from pure Ni, Co, Mn, Sn, In elements ($\ll$ 99.99%) by induction casting. Then, cylindrical central part of the ingot was cut out with a spark cut machine, placed in a crucible, remelted and directionally solidified (Bridgman) at a rate of 10 mm/h in a Lora up to 1700 furnace unit. Directional solidification was applied, since it appears advantageous in comparison with more conventional casting routes in terms of curbed segregation, and thus, it necessitates less time spent on homogenization heat treatment [24]. It also provides favourable material for investigation of ordering effects, because it produces large grains (Fig. 1a) convenient for microstructure analysis, while simultaneously maintaining sufficient density of grain boundaries (vacancy sinks), unlike more conventional polycrystalline or single-crystalline specimens unable to reconcile both demands.

Scanning electron microscopy (SEM) and electron back-scatter diffraction (EBSD) observations showed the absence of secondary precipitation phases, while the microstructure was typically martensitic at room temperature (Fig. 1b). The as-cast ingot had been close to (001) orientation (Fig. 1c).

Following solidification, the ingot was encapsulated in a quartz ampoule under vacuum and annealed at 1270 K for 72 h followed by water quenching (WQ). Such prepared sample is hereafter referred to as 1220WQ. Additional heat treatment entailing heating up to 1070 K and then slow cooling with the furnace down to 770 K for 1 h followed by WQ were also performed on part of the 1220WQ alloy, and it produced sample denoted henceforward as 1070SLC.

The compositions of elaborated alloys were determined according to X-ray energy dispersive spectroscopy (EDS) analyser fitted to the FEI ESEM XL30 scanning electron microscope (SEM). The microstructure was studied using Tecnai G2 (200 kV) transmission electron microscope equipped with energy dispersive spectrometer (EDX). Thin foils for TEM inspection were prepared at 240 K using TenuPol-5 double jet electropolisher and an electrolyte made up of nitric acid ($\frac{1}{3}$ vol.) and methanol ($\frac{2}{3}$ vol.) [17]. Powder X-ray diffraction (XRD) patterns were collected at 420 K with Siemens D5000 diffractometer equipped with an Oxford continuous flow cryostat, and a diffracted beam graphite monochromator. The application of diffracted beam monochromator was important to effectively eliminate undesirable fluorescence radiation (effects) from the Mn and Co atoms in the alloys for the used Cu K_α radiation. Tungsten powder (APS 5–6 μm, Puratronic, 99.999%) was used as an internal standard. The XRD patterns were analysed using the FullProf [25, 26] software based on the Rietveld method. Thermal effects were investigated at the temperature range of 293–1423 K by differential scanning calorimetry (DSC) employing the DSC 404 F1 Pegasus, Netzsch instrument. The heating/cooling rate was 10 K min^{-1}. The DC mass magnetic susceptibility (and magnetization) was measured in the temperature range from 2 K up to 380 K and in the magnetic field of 5 mT (and 5 T) using vibrating sample magnetometer (VSM) option of the Quantum Design Physical Property Measurement System (PPMS-9).

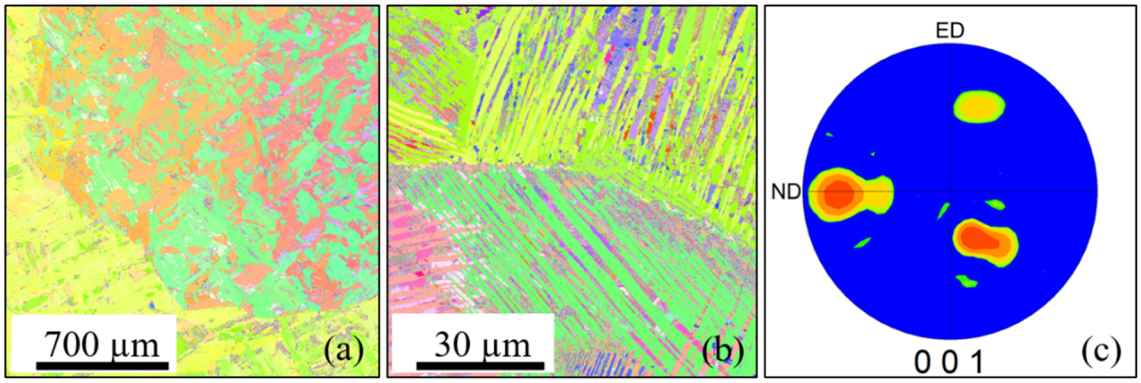

Figure 1 Electron back-scatter diffraction images (**a**, **b**) taken from the cross section of the as-solidified $Ni_{49}Co_1Mn_{37.5}Sn_{6.5}In_6$ alloy and a pole figure (**c**) illustrating that the growth direction is closely parallel to the ⟨001⟩ direction.

Results and discussion

Microstructure/structure

In the as-solidified (Bridgman) state, the $Ni_{49}Co_1Mn_{37.5}Sn_{6.5}In_6$ alloy had a non-uniform microstructure in terms of structural phase composition. Inspection of a thin foil with TEM exposed coexistence of austenite phase with the $L2_1$ structure (Fig. 2a) and martensite with three different types of modulated structures, namely: 4O (Fig. 2b), 10M (Fig. 2c) and 6M (Fig. 2d). All the structures have been identified according to the diffraction patterns (SADPs) taken along the $[111]_{L21}$, $[012]_{4O}$, $[210]_{10M}$ and $[210]_{6M}$ zone axes, given for illustration in Fig. 2. Chemical composition checked with EDX corroborated composition variation in micro-areas. The following stoichiometries (at.%) have been elaborated in the respective martensite micro-areas: 10M—$Ni_{51.2}Co_{0.7}Mn_{37.9}Sn_{5.9}In_{4.2}$ (e/a = 8.21); 6M—$Ni_{51.5}Co_{0.9}Mn_{37.7}Sn_{5.5}In_{4.5}$ (e/a = 8.22); 4O—$Ni_{49.2}Co_{1.2}Mn_{37.7}Sn_{6.0}In_{5.9}$ (e/a = 8.08); $L2_1$—$Ni_{48.5}Co_{0.9}Mn_{35.5}Sn_{8.4}In_{6.7}$ (e/a = 7.95). In order to improve homogeneity, the alloy was heat treated at 1220 K for 72 h and then WQ. After quenching, the 1220WQ alloy attained the successive composition: $Ni_{49.4}Co_{1.3}Mn_{37.4}Sn_{5.9}In_6$ (e/a = 8.09). Secondary heat treatment carried out at 1070 K for 1 h followed by SLC produced the 1070SLC specimen with almost unaltered composition (within the EDX error limit ± 0.01 at.%) with respect to the initial 1220WQ alloy, i.e. $Ni_{49.3}Co_{1.2}Mn_{37.4}Sn_{6.1}In_6$ (e/a = 8.08).

Regardless of the consistency in composition, the martensite structure has changed between the 1220WQ and 1070SLC alloys. Whereas the 1220WQ alloy is found at room temperature with the 6M martensite (Fig. 3d, e), confirmed with SADP acquired along the [210] zone axis, the 1070SLC alloy has at room temperature the 10M martensite structure (Fig. 3i, j), indexed according to the [210] electron beam direction. No other precipitate phases nor other martensites and austenite have been found in both alloys confirming that chemical homogeneity had been attained on a microscale. Since the

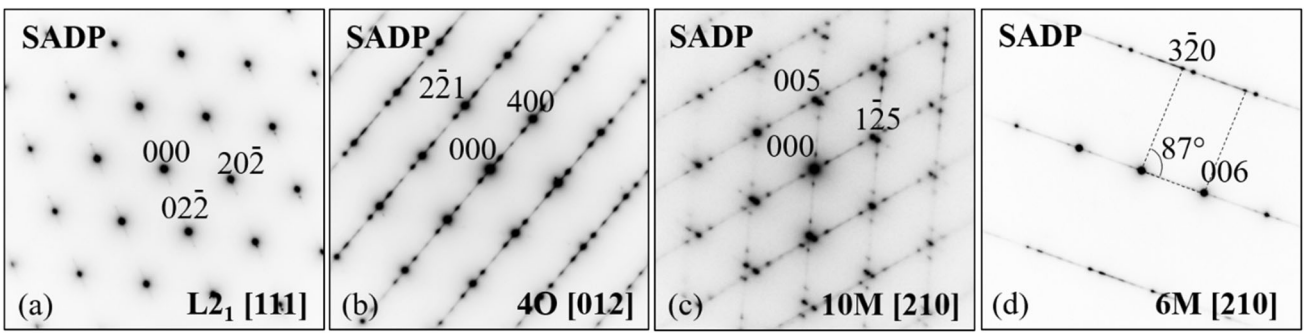

Figure 2 Selected area electron diffraction patterns (SADPs) taken at room temperature from the austenite (**a**) and martensite (**b**–**d**) phases present in the as-directionally solidified $Ni_{49}Co_1Mn_{37.5}Sn_{6.5}In_6$ alloy.

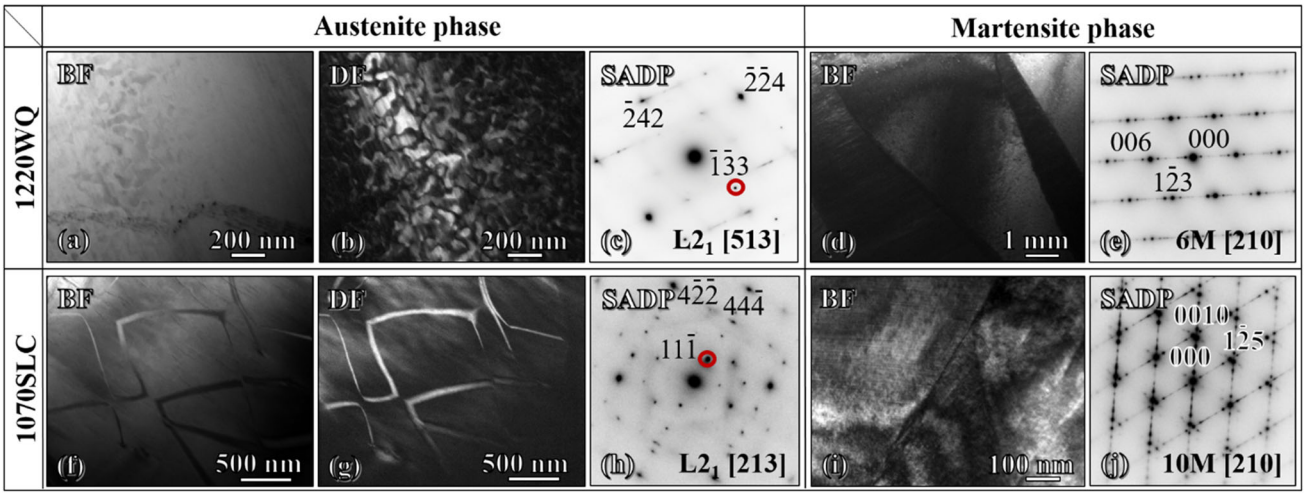

Figure 3 Bright field (BF), dark field (DF) micrographs and selected area electron diffraction patterns (SADPs) taken at room temperature from the austenite (**a**–**c** and **f**–**h**) and martensite (**d**, **e** and **i**, **j**) phases present in the 1220WQ (**a**–**e**) and 1070SLC (**f**–**j**) alloys.

compositional non-uniformity cannot account for the change in martensite structure, both samples have been examined against a change in the degree of ordering imposed by WQ and SLC. Qualitatively, the difference in the degree of order between the 1220WQ and 1070SLC alloys is clear from Fig. 3a–c, f–h. The figure shows bright field (BF)—(a, f)—and dark field (DF)—(b, g)—micrographs along with the corresponding SADPs—(c, h)—taken during in situ TEM heating up to 420 K, well above the austenite finish (A_f) temperature (disclosed later), at which temperature all the images were recorded. Figure 3a, b shows DO3-type antiphase domains (APDs) better visible in DF mode (Fig. 3b) registered with the $(\bar{1}\bar{3}\bar{3})$ reflection in the 1220WQ alloy. The size of APDs is much smaller relative to the coarse B2-type domain structure developed by slow cooling in the 1070SLC alloy—(Fig. 3f, g), well shown by DF (Fig. 3g) based on the $(11\bar{1})$ spot, where the density of antiphase boundaries (APBs) is much less pronounced (it is to be noted that the observed long-range ordering is the average through the sample thickness [27]). For more quantitative evaluation, the TEM experiments have been complemented with in situ heating XRD measurements at the same temperature. It has been confirmed (Fig. 4) that at 420 K the compounds are single austenite phase of the Heusler $L2_1$-type cubic structure (space group $Fm\bar{3}m$) [28, 29]. It is expected that in this structure the Ni/Co atoms should occupy the 8*c* (0.25, 0.25, 0.25), the Sn and In atoms the 4*b* (0.5, 0.5, 0.5) and Mn atoms 4*a* (0, 0, 0) and partly 4*b* (0.5, 0.5, 0.5) sites. Since the atomic scattering factors of heavy Sn and In are much larger than Ni, Co and Mn ones, it was possible to determine the occupancies of different available sites with Sn and In atoms and from the same reasons it was impossible to distinguish Sn from In atom and Ni from Mn or Co atoms. It was found, in all three samples (as-cast, 1220WQ and 1070SLC), that Sn/In atoms partially occupy the 4*a* (0, 0, 0) and 4*b* (0.5, 0.5, 0.5) sites. No Sn or In atoms were detected on 8*c* (0.25, 0.25, 0.25) sites. The results are shown in Table 1.

Thermal effects

The characteristic martensite (austenite) start M_s (A_s) and finish M_f (A_f) temperatures have been extracted from the DSC curves (Fig. 5a) by the tangent method and are presented in Table 2. The forward and reverse MT peak temperatures ($T_p^{A\leftrightarrow M}$) and the transformation entropy changes ($\Delta S_{MT}^{A\leftrightarrow M}$) computed from DSC thermograms according to the formula: $\Delta S_{MT}^{A\leftrightarrow M} = L/T_p^{A\leftrightarrow M}$, where L is the latent heat of the transformation, are provided in the same table too.

The DSC peaks taken for the as-cast alloy on forward and reverse MT are broad and show tailing effects. On the other hand, the peaks recorded for the 1220WQ and 1070SLC samples are more sharp and better defined. The M_s temperature is found to increase by ~ 10 K following SLC relative to the 1220WQ specimen, whereas it remains highest in the as-cast state. The transformation hysteresis (A_f–M_s) increases with progressing heat treatment, which may indicate some hindrances to elastic strain

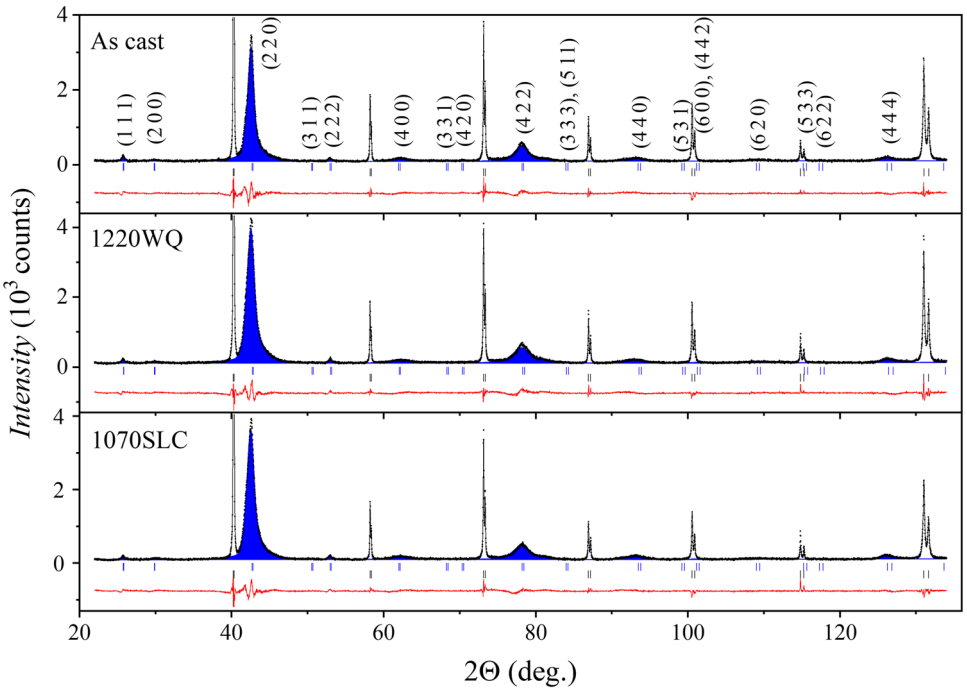

Figure 4 Powder X-ray diffraction patterns of the as-cast, 1220WQ and 1070SLC compounds at 420 K (solid black circles) with the results of the Rietveld refinement denoted by solid black line (best fit) and contribution of austenite (blue areas) phase. The calculated positions of the reflections for cubic austenite (space group: $Fm\bar{3}m$) and tungsten standard (space group $Im\bar{3}m$) phases are shown as upper blue and lower black sets of vertical bars just below the pattern, respectively. Only the peaks of as-cast austenite phase (in uppermost panel) are indexed. The lower solid red line represents the difference curve between experimental and fitted patterns.

Table 1 Lattice site occupancy (%) and lattice parameter of austenite (a_{L2_1}) at 420 K in the as-directionally solidified $Ni_{50}Co_1Mn_{38.5}Sn_{6.5}In_6$ and heat-treated 1220WQ and 1070SLC alloys

Compd.	As-cast	1220WQ	1070SLC
4*a* (0, 0, 0)			
Mn	83.1 ± 1.4%	84.2 ± 1.7%	83.5 ± 1.5%
Sn/In	16.9 ± 1.4%	15.8 ± 1.7%	16.5 ± 1.5%
4*b* (0.5,0.5,0.5)			
Mn	66.9 ± 1.4%	65.8 ± 1.7%	66.5 ± 1.5%
Sn/In	33.1 ± 1.4%	34.2 ± 1.7%	33.5 ± 1.5%
a_{L2_1} (Å)	5.9843 ± 0.0004	5.9787 ± 0.0005	5.9829 ± 0.0005

energy. Possibly, this finds manifestation in the form of spikes on the DSC curve measured on heating for the 1070SLC alloy. Such spikes are typically attributable to the advancement of the austenite and martensite phase interface and depend on various factors including ordering [30].

Thus, in order to establish the ordering temperature the 1220WQ alloy was DSC scanned from room temperature up to 1400 K on two consecutive heating/cooling cycles. A distinct endothermic peak indicating order–disorder transformation [31] found on heating for, e.g., Ni–Mn–In around 965 K [3] has not been observed on this occasion around such temperatures; nonetheless, an endothermic peak has been found at 1258 K immediately prior to the melting point (Fig. 5b). It is shown magnified for better illustration in the inset I in Fig. 5b. What more the first heating run revealed two exothermic peaks, encircled and magnified for visibility in the inset II in Fig. 5b, in the temperature range ca. 750–1025 K, which might be related to ordering process [3]. The peaks were a one-time occurrence only on the first heating run, and the consecutive cooling and subsequent second cycle (not shown) were deprived of any

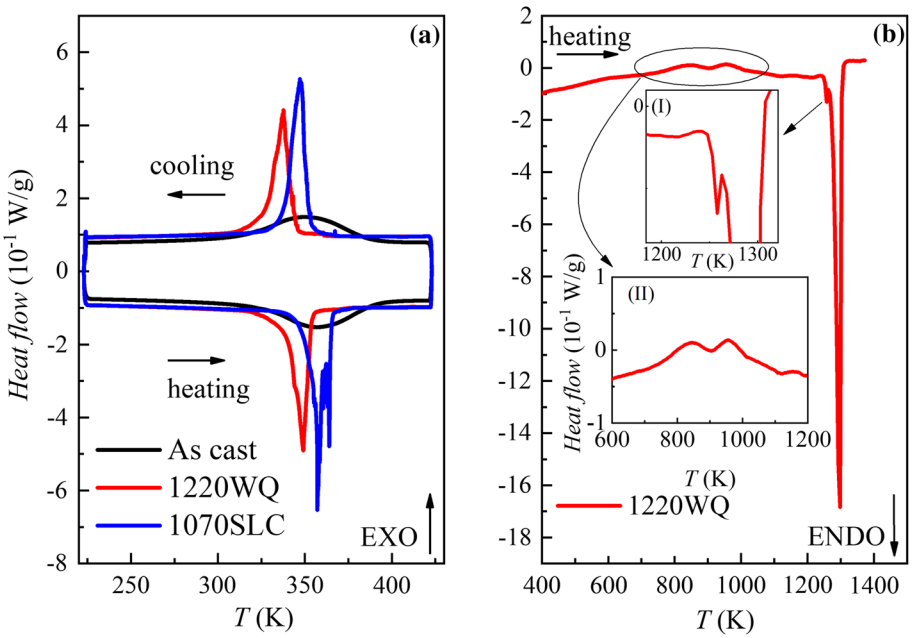

Figure 5 Differential scanning calorimetry (DSC) curves of the as-cast, 1220WQ and 1070SLC alloys upon heating and cooling within the 225–425 K temperature window (**a**) and DSC recorded upon heating up to 1400 K for the 1220WQ alloy (**b**).

Table 2 Characteristic martensite start (M_s), martensite finish (M_f) and austenite start (A_s), austenite finish (A_f) temperatures, the transformation hysteresis (A_f–M_s) and transformation interval (M_s–M_f); (A_f–A_s), the transformation peak temperatures ($T_p^{A\to M}$, $T_p^{M\to A}$) and the entropy changes upon the forward ($\Delta S_{MT}^{A\to M}$) and reverse ($\Delta S_{MT}^{M\to A}$) martensitic transformation

	M_s (K)	M_f (K)	A_s (K)	A_f (K)	A_f–M_s (K)	M_s–M_f (K)	A_f–A_s (K)	$T_p^{A\to M}$ (K)	$T_p^{M\to A}$ (K)	$\Delta S_{MT}^{A\to M}$ (J/kgK)	$\Delta S_{MT}^{M\to A}$ (J/kgK)
As-cast	389	309	324	393	4	80	69	350	359	66.6	55.1
WQ	345	326	338	354	9	19	16	337	349	74.2	74.6
SLC	354	337	349	366	12	17	17	347	357	76.1	72.8

peaks in similar temperature range. The melting point is found around 1298 K in agreement with the literature [24].

Magnetization

The thermomagnetization curves measured in the applied field of 5 mT for the as-cast, 1220WQ and 1070SLC alloys are shown in Fig. 6a. Regardless of the type of thermal treatment, all the alloys appear to undergo MT from a paramagnetic austenite to a paramagnetic/weakly magnetic martensite, and the magnetic susceptibility in martensite is seemingly nonzero (inset in Fig. 6a). The martensite phase is stable to a T_P temperature, the low temperature maximum on the ZFC curve below which the ZFC and FC curves separate (Fig. 6a). Below the T_P, all the alloys show magnetic inhomogeneity suggested by the irreversibility of the thermomagnetic ZFC and FC/FH curves. The T_P for the as-cast alloy is determined from the maximum on the ZFC curve at 172 K, whereas in the case of the homogenized and thermally treated 1220WQ and 1070SLC alloys it is found at 132 K and 141 K, respectively. Below the T_P a range of complex, intricate magnetic states are expected in typical MSMA, and these may include ferromagnetic, antiferromagnetic, superparamagnetic and spin glassy states [7, 14–16].

From the minimum of the FC dM/dT curve, the T_C^M has been found at 127 K for the as-cast alloy and at 116 K for both the 1220WQ and 1070SLC alloys. In addition, the FC dM/dT curve taken for the as-cast alloy showed a clear minimum at 323 K, indicating the T_C^A. Instead, the first derivatives taken for the

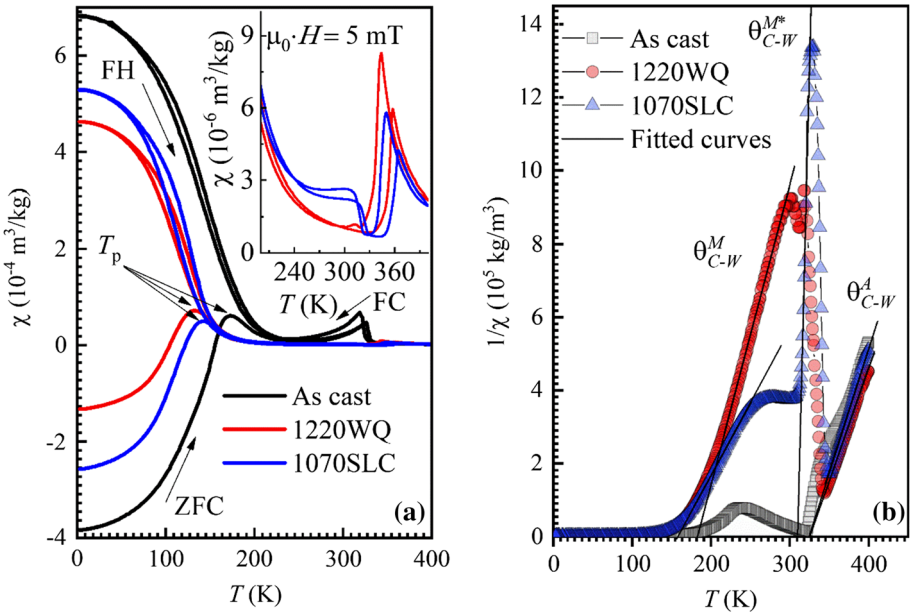

Figure 6 Magnetic susceptibility (zero field cooled, field cooled, field heated)—χ (**a**) and inverse magnetic susceptibility (FC)—$1/\chi$ (**b**) versus temperature for the as-cast, 10220WQ and 1070SLC alloys under the applied field of 5×10^{-3} T. Linear fitting of the Curie–Weiss law is indicated (by solid black lines) in (**b**).

1220WQ and 1070SLC had only maximums at 339 and 343 K, respectively, attributed to the forward T_{MT}, in consistence with DSC (Table 2). In fact, a vague minimum ($dM/dT < 0$) was discerned for the 1070SLC at 319 K, corresponding to the sudden upturn of the curve (inset in Fig. 6a), possibly pointing to the Curie transformation in this alloy; nonetheless, it was not distinct enough for an unambiguous identification. This implies that the $T_C^A < M_s$ and hence the MT obscures the T_C^A estimation. Assuming then that both austenite and martensite phases are paramagnetic at the onset of MT, the Curie–Weiss relation: $\chi = \frac{C}{T-\theta_{CW}} \rightarrow \frac{1}{\chi} = \frac{T}{C} - \frac{\theta_{CW}}{C}$, where C is the Curie constant and θ_{CW} denotes the paramagnetic Curie–Weiss temperature, has been applied and from the linear fit to the $1/\chi$ versus T dependencies (Fig. 6b) we have found the θ_{CW} and the effective magnetic moment (μ_{eff}) per "compound" atom ($\mu_{eff} = \sqrt{\frac{3Mk_BC}{\mu_0 N_A}}$, where M stands for the molar mass, k_B is the Boltzmann constant, whereas μ_0 is the magnetic permeability of vacuum and N_A is the Avogadro's number). Obtained results (Table 3) uncover that the μ_{eff} in the austenite phase (μ_{eff}^A) is by somewhat 0.2 μ_B lower relative to the as-cast and the 1220WQ samples. On the other hand, the μ_{eff} of the martensite state is the highest in the as-cast alloy, lower in the 1070SLC and the lowest in the 1220WQ specimen. The θ_{CW} temperatures of the austenite phase (θ_{CW}^A) in the 1220WQ and 1070SLC alloys are close to one another and are equal to 326 K and 328 K, accordingly. In the martensite phase, the θ_{CW}^M in the 1220WQ alloy is 25 K above the θ_{CW}^M in the 1070SLC sample. Interestingly, the $1/\chi$ versus T for the 1070SLC alloy shows two linear ranges, which clearly differ in slope, within the temperatures 150–325 K. This is less apparent in the case of the 1220WQ sample; nonetheless, a trace of the second linear range is visible around 300 K in this alloy. Linear fitting within this range allows for determining μ_{eff}^{M*} and θ_{CW}^{M*}, denoted with asterisk for distinction. From the isothermal magnetization measured at 50 K, it appears that the magnetic moment per formula unit under the magnetic field of $\mu_0 \cdot H = 2$ T in the 1220WQ alloy is $M_{sat}^{50\,K} = 0.6$ μ_B/f.u., whereas in the 1070SLC alloys it assumes $M_{sat}^{50\,K} = 0.7$ μ_B/f.u. The spontaneous magnetization determined at this temperature ($M_{sp}^{50\,K}$) from the Arrott plots (M^2 vs. H/M) for the 1220WQ is equal to 15.7 Am^2/kg and 16.3 Am^2/kg for the 1070SLC alloy (Table 3).

In order to account for the fact that structural and magnetic transformations overlap, what makes it difficult to discern the clear transformation stages under low $\mu_0 \cdot H$, additional fitting to the better resolved isofield ($\mu_0 \cdot H = 5$ T) thermomagnetization curves (Fig. 7) have been performed to corroborate the magnetic states of martensite and austenite across the MT. The fitting has been executed according to the Curie–Weiss formula; i.e. $M = n\frac{N_A}{3k_B}\mu_{eff}^2\frac{(\mu_0 H)}{T-\theta_{CW}}$,

Table 3 Spontaneous magnetization ($M_{sp}^{50\,K}$) determined from the Arrott plots at 50 K, effective magnetic moments (μ_{eff}) per "compound" atom in Bohr magnetons (μ_B) and the paramagnetic Curie–Weiss (θ_{CW}) temperatures derived from the linear fitting of the Curie–Weiss law to the $1/\chi$ versus T curves for the as-cast, 10220WQ and 1070SLC alloys

	$M_{sp}^{50\,K}$ (Am^2/kg)	μ_{eff}^{A} (μ_B)	μ_{eff}^{M} (μ_B)	μ_{eff}^{M*} (μ_B)	θ_{CW}^{M} (K)	θ_{CW}^{M*} (K)	θ_{CW}^{A} (K)
As-cast	–	2.6 ± 0.3	4.7 ± 0.5	–	190	–	315
WQ	15.7	2.6 ± 0.2	2.2 ± 0.2	1.7 ± 0.8	182	250	326
SLC	16.3	2.4 ± 0.2	3.2 ± 0.3	0.8 ± 0.2	157	308	328

where θ_{CW} is the fitted paramagnetic Curie–Weiss temperature, n number of moles of Mn per gram-atom, whereas μ_{eff} is given by the following relation: $\mu_{eff} = g\mu_B\sqrt{J(J+1)}$, where g (g = 2) is Lande's factor and J is the fitted angular momentum quantum number. The fitting was performed at the distinct temperature ranges of 180–300 K for martensite ($T_C^M < T < M_f$) and 346 (355)–400 K ($T > M_s$) for the austenite in both the 1220WQ (1070SLC) alloys. Results are summarized in Table 4.

Unsurprisingly, given the most likely paramagnetic states of the transforming phases, the characteristic transformation temperatures display almost null dependence on the applied magnetic field (Fig. 8). On the contrary, the T_p decreases with increasing $\mu_0 \cdot H$ until it is eventually suppressed under 5 T.

Since, above the T_p, the isothermal magnetization curves (Fig. 9) display none or marginal hysteresis

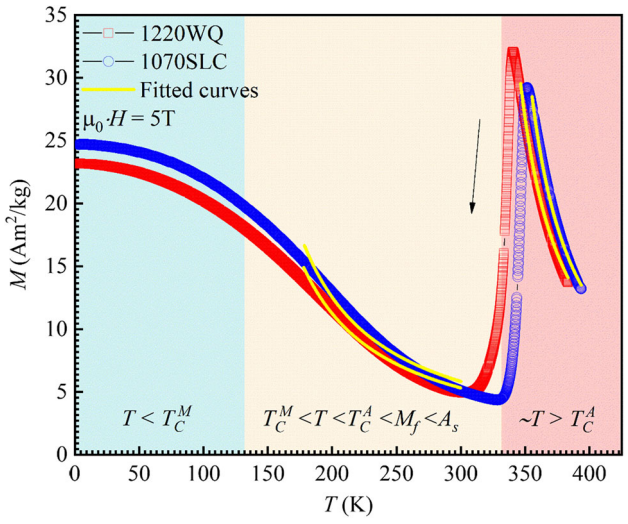

Figure 7 Isofield ($\mu_0 \cdot H$ = 5 T) thermomagnetization curves measured for the 1220WQ and 1070SLC alloys. The Curie–Weiss function fittings to the curves are indicated with yellow lines.

Table 4 Austenite (θ_{CW}^{A}) and martensite (θ_{CW}^{M}) paramagnetic Curie–Weiss temperature and angular momentum quantum number (J) obtained by fitting the Curie–Weiss function to the magnetization versus temperature curves measured at 5 T

	θ_{CW}^{A} (K)	J^A	θ_{CW}^{M} (K)	J^M
WQ	313	0.532 ± 0.001	110	0.538 ± 0.002
SLC	321	0.527 ± 0.001	113	0.570 ± 0.002

loops, the existence of superparamagnetic exchange has been probed at 150 K, 200 K and 250 K, i.e. within the temperature range $T_C^M < T < M_f$. The curves (Fig. 9) have been fitted according to the modified Langevin function, which traces magnetization of ferromagnetic clusters and which is outlined as follows: $M(H) = \frac{N}{\rho} \cdot \mu L(\xi) + \chi_0 H$, where ρ denotes alloy's density, N stands for ferromagnetic clusters' density, while μ is the mean saturation magnetic moment per cluster, whereas $L(\xi) = \coth(\xi) - 1/\xi$ is the Langevin function, where $\xi = \mu_0\mu H/k_B T$ and χ_0 is magnetic susceptibility of the matrix. The results are given in Table 5.

Discussion

From the microstructural analysis, it comes to light that despite slow solidification rates (10 mm/h) the as-cast $Ni_{49}Co_1Mn_{37.5}Sn_{6.5}In_6$ alloy is not free from some composition fluctuation. It then results in the co-occurrence at room temperature of austenite ($L2_1$) and three different types of modulated martensite structures (4O, 10M and 6M), which is explained through a well-established dependence of martensite structure and MT temperatures on the valence electron concentration (e/a) [11, 32]. Due to inhomogeneity, the DSC peaks for the as-cast alloy are broad, since the MT temperature is smeared over a wide

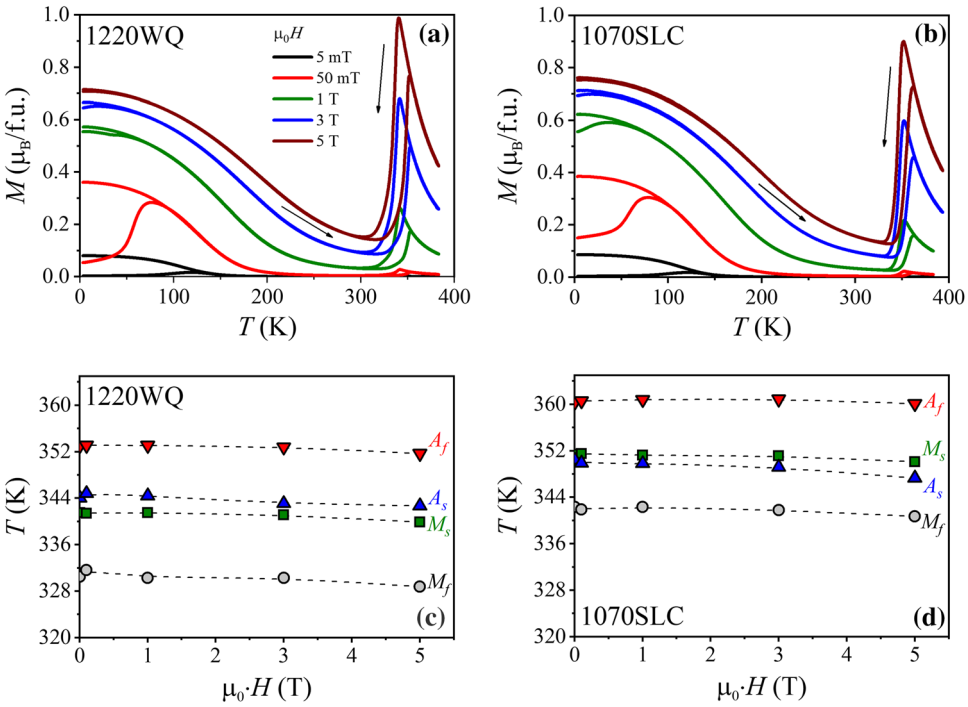

Figure 8 Magnetization (M) in Bohr magnetons per formula unit (μ_B/f.u.) versus temperature curves measured at 5 mT, 50 mT, 1 T, 3 T and 5 T for the 1220WQ (**a**) and 1070SLC (**b**) alloys and the corresponding characteristic M_s, M_f, A_s, A_f temperature dependencies on the applied magnetic field (**c**) and (**d**), respectively.

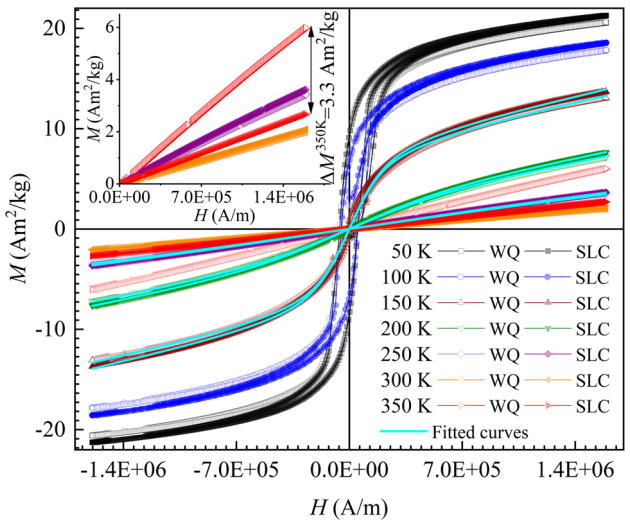

Figure 9 Isothermal magnetization curves measured at various temperatures from 50 to 350 K for the 1220WQ and 1070SLC alloys. Fitting of the Langevin function at 150 K, 200 K and 250 K is indicated (by solid lines).

temperature window. Homogenization heat treatment concluded with WQ rectifies inhomogeneity and produces a single-phase martensite with 6M structure in the 1220WQ alloy. Additional heat treatment followed with furnace cooling does not upset chemical homogeneity; nonetheless, it modifies the extent of the degree of order. From the DSC (Fig. 5b), it is clear that this treatment has been carried out above (1070 K) the temperature range where the ordering takes place and thus unlike the rapidly quenched 1220WQ the 1070SLC alloy has been allowed to attain equilibrium ordering. This is well confirmed with DF imaging (Fig. 3b, g), which uncovers significant size difference in APDs microstructure. Higher degree of order then translates into a different martensite structure, namely 10M in the 1070SLC alloy in consistence with the literature [11, 17]. Additional evidence for improved ordering is supplied by XRD measurements showing that more Mn/In(Sn) atoms are misplaced in the 1220WQ alloy as opposed to the as-cast and 1070SLC alloys.

The DSC peaks for both heat-treated alloys are better resolved than in the case of the as-cast alloy, and they are displaced with respect to one another by ca. 10 K in favour of the 1070SLC alloy ($T_{MT}^{1070SLC} > T_{MT}^{1220WQ}$). Interestingly, for the as-cast alloy the $\Delta S_{MT}^{A\rightarrow M} > \Delta S_{MT}^{M\rightarrow A}$. On the forward MT, only 17.5% of the transforming phase in this alloy is ferromagnetic ($f_{ferro.}^{A} = T_C^A - M_f/M_s - M_f$), whereas on the reverse MT martensite transforms directly into a paramagnetic austenite ($T_C^A > A_s$). In principle, when accounting for the magnetic contribution, this should then lead to opposite results. Therefore, herein this effect is ascribed to partial irreversibility of the

Table 5 Saturation magnetization at $\mu_0 \cdot H = 2\,\mathrm{T}$ ($M_{\mathrm{sat}}^{2\,\mathrm{T}}$), cluster magnetic moment (μ_c), ferromagnetic cluster density (N) and magnetic susceptibility (χ_0), the latter three obtained from the fitting of the Langevin function at 150 K, 200 K and 250 K

	T (K)	$M_{\mathrm{sat}}^{2\,\mathrm{T}}$ (Am^2/kg)	μ_c (μ_B)	N (m^{-3})	χ_0 (m^3 kg^{-1})
WQ	150	13.0	20.5×10^2	4.39×10^{20}	3.4×10^{-6}
	200	7.19	8.52×10^2	4.22×10^{20}	2.8×10^{-6}
	250	3.45	4.27×10^2	3.37×10^{20}	1.7×10^{-6}
SLC	150	13.7	19.8×10^2	4.81×10^{20}	3.5×10^{-6}
	200	7.65	8.86×10^2	4.28×10^{20}	2.9×10^{-6}
	250	3.64	6.29×10^2	1.35×10^{20}	1.9×10^{-6}

transformation due to homogeneity issues in the as-cast alloy. In contrast, $\Delta S_{\mathrm{MT}}^{\mathrm{A}\leftrightarrow\mathrm{M}}$ values are similar on the direct and reverse MT for both the 1220WQ and the 1070SLC alloys and amount to an average of 74.4 J/kg K.

At the first approximation according to the thermomagnetic measurements, the austenite and martensite phases in both alloys appear paramagnetic throughout the MT. Hence, little to nothing influence of the magnetic field on the MT temperatures, which can be justified based on the Clausius–Clapeyron relationship: $\frac{\Delta H}{\Delta T} = \frac{\Delta S}{\Delta M} \rightarrow \Delta T = \left(\frac{\Delta M}{\Delta S}\right)\Delta H$. When adopting ΔS = 74.4 J/kg•K, and from Fig. 7 determining ΔM at $\mu_0 \cdot H$ = 5 T around M_s/M_f as 27 and 25 J/T kg (= emu/g) for the 1220WQ and 1070SLC alloys, respectively, it hence leads to $\Delta T^{1220\mathrm{WQ}}$ = 1.9 K and $\Delta T^{1070\mathrm{SLC}}$ = 1.7 K, which is in agreement with experiment. Although the obtained μ_{eff} and the J values ($\sim$ 0.5) for austenite (Table 3 and 4), the latter much lower than typical values for ferromagnetic MSMA, where $gJ\mu_B = 4\mu_B$ assuming the magnetic moment is chiefly confined on Mn atoms [7], leave no doubt to the paramagnetic nature of austenite across MT, the magnetic constitution of martensite is somewhat more intricate and it appears to benefit from increased ordering. Whereas the $\mu_{\mathrm{eff}}^{\mathrm{A}}$ in the 1220WQ alloy is slightly larger, by 0.4 μ_B, than $\mu_{\mathrm{eff}}^{\mathrm{M}}$, the opposite is true for the 1070SLC and the difference is twice the magnitude—0.8 μ_B (Table 3). The ferromagnetic cluster densities determined for both alloys are lower (Table 5) than typical values ($1.78 \pm 0.01 \times 10^{25}$ m^{-3}) reported for Ni–Co–Mn–Sn base MSMA [15], while the mean magnetic moment is slightly larger than the moment ($503 \pm 3\ \mu_B$) found in alloys with superparamagnetic exchange [15, 16]. This may indicate a finite ferromagnetic component below M_f in both the 1220WQ and the 1070SLC alloys. Whereas at 150 K and 200 K the N and μ in both alloys are at the similar level, at 250 K they differ more significantly. On the whole, the magnetization of the 122WQ alloy above the $> T_C^{\mathrm{A}}$ is larger than the magnetization of the 1070SLC alloy, which may derive from the increasing M_s—T_C^{A} temperature difference. On the contrary at lower temperatures, the magnetization of the 1070SLC alloys is larger than magnetization of the 1220WQ suggesting a stronger ferromagnetic exchange due to atomic ordering. Larger μ noted at 250 K in the 1070SLC alloy together with the doubled linear curve in the $1/\chi$ versus T may then most likely arise from a retained ferromagnetic austenite residing within the paramagnetic martensite matrix. At lower temperatures below the T_C^{A} ($\sim$ 319 K), the retained austenite orders ferromagnetically and since ferromagnetic exchange is promoted by increasing ordering, at lower temperature range the 1070SLC alloy shows higher magnetization than the 1220WQ alloy [21]. Below the T_p, most likely antiferromagnetic and ferromagnetic exchange coexist and the T_p is suppressed with increasing $\mu_0 \cdot H$.

From the discussion, it emerges that the primary driving force for the observed T_{MT} temperature shift between the 1220WQ and the 1070SLC alloys, regardless of the magnetic state of martensite, derives from the changes in microstructure imposed by heat treatment. In analogy to more conventional magnetic and non-magnetic shape memory alloys, the T_{MT} temperature shift may arise on the one hand from a change in the free energy difference across the MT. Acknowledging that the MT is diffusionless and that martensite inherits atomic ordering of the parent phase, its relative stability may thus be affected subject to the extent of retained disorder [33]. Assuming a linear dependence between the T_{MT} and

the order parameter s, found for, e.g., Ni–Mn–Ga [34, 35], the following relationship can be then established: $\delta\Delta G^{A\leftrightarrow M} = \Delta S_{MT}^{A\leftrightarrow M} \cdot \alpha \cdot \delta s$, where α is the slope of the T_{MT} versus s dependence. Henceforth, depending on the configurational order the $\Delta S_{MT}^{A\leftrightarrow M}$ and s may take different values adjusting the temperature stability range and hence T_{MT}. On the other hand within a more mechanistic approach, the change in T_{MT} in response to ordering may be ascribed to quenched-in vacancies arrested at domain interfaces, thus pining their movement [30]. Also, the influence of APD size on twinning stress should not be overlooked. Twinning stress in some systems is found to decrease with decreasing APD size [36]. Recent experiments showed that for the same temperature the stress necessary to trigger MT was higher in the more ordered Ni–Co–Mn–In single crystal [37]. The effect may derive from the intrinsic characteristics of MT. Since the nucleation and propagation of MT rest on the formation of compatible habit planes between austenite and martensite, typically involving production of fine, microlaminated twin structures at interface than T_{MT} might be susceptible to twinning stress. More recently, we have shown a 29 K shift in the A_s temperature in mechanically stabilized martensite in Ni–Mn–Sn single crystal as opposed to 1 K shift in Ni–Mn–Ga, where the systems differ in twinning stress by a factor of ~ 9 [38].

Overall heat treatment-induced martensite stabilization in the $Ni_{49}Co_1Mn_{37.5}Sn_{6.5}In_6$ alloy most likely appears to develop from microstructural changes influencing the free energy difference across MT and the twinning stress through interaction with APDs, whose size is modified by heat treatment.

Summary and conclusions

The as-directionally solidified $Ni_{49}Co_1Mn_{37.5}Sn_{6.5}In_6$ alloy was subjected to annealing at 1220 K followed by water quenching, and then it was subjected to annealing for 1 h at 1070 K followed by slow cooling. In response to water quenching, the alloy developed the 6M martensite structure and coarse APBs' microstructure, whereas slow cooling resulted in the 10M martensite and fine APBs. The martensitic transformation temperature increased ($\Delta T_{MT} = 10$ K) following slow cooling relative to the as-quenched state. During the martensitic transformation, irrespective of the thermal history, the paramagnetic austenite transforms into weakly magnetic martensite, whose magnetic moment is amplified by slow cooling ($\Delta\mu_{eff}^{M} = 1\mu_B$). The observed behaviours are attributed to the increase in the degree of ordering, which regardless of the magnetic state stabilizes martensite through the interaction with the free energy difference and through the influence of APBs on twinning stress.

Funding

This study was funded by the Polish National Centre for Research and Development, NCBiR (grant number PBS/A5/36/2013), and partially by the Faculty of Physics and Applied Computer Science AGH UST statutory tasks (within subsidy of Ministry of Science and Higher Education). Dr Robert Chulist (IMMS PAS) is acknowledged for EBSD measurements.

Compliance with ethical standards

Conflict of interest The authors declare that they have no conflict of interest.

References

[1] Kustov S, Corro ML, Pons J, Cesari E (2009) Entropy change and effect of magnetic field on martensitic transformation in a metamagnetic Ni–Co–Mn–In shape memory alloy. Appl Phys Lett 94:191901-1–191901-3

[2] Barandiaran JM, Chernenko VA, Cesari E, Salas D, Gutierrez J, Lazpita P (2013) Magnetic field and atomic order effect on the martensitic transformation of a metamagnetic alloy. J Phys Condens Matter 25:484005–1–484005-6

[3] Sanchez-Alarcos V, Recarte V, Perez-Landazabal JI, Cesari E, Rodriguez-Velamazan JA (2016) Long-range atomic order

and entropy change at the martensitic transformation in a Ni–Mn–In–Co metamagnetic shape memory alloy. Entropy 16:2756–2767. https://doi.org/10.3390/e16052756

[4] Recarte V, Perez-Landazabal JI, Sanchez-Alarcos V, Rodriguez-Velamazan JA (2012) Dependence of the martensitic transformation and magnetic transition on the atomic order in Ni–Mn–In metamagnetic shape memory alloys. Acta Mater 60:1937–1945

[5] Sutou Y, Imano Y, Koeda N, Omori T, Kainuma R, Ishida K, Oikawa K (2004) Magnetic and martensitic transformations of NiMnX (X = In, Sn, Sb) ferromagnetic shape memory alloys. Appl Phys Lett 85(19):4358–4360

[6] Sanchez-Alarcos V, Perez-Landazabal JI, Recarte V, Lucia I, Velez J, Rodriguez-Velamazan JA (2013) Effect of high-temperature quenching on the magnetostructural transformations and the long-range atomic order of Ni–Mn–Sn and Ni–Mn–Sb metamagnetic shape memory alloys. Acta Mater 61:4676–4682

[7] Plogmann S, Schlatholter T, Braun J, Neumann M, Yarmoshenko YM, Yablonskikh MV, Shreder EI, Kurmaev EZ, Wrona A, Ślebarski A (1999) Local moments in Mn-based Heusler alloys and their electronic structures 60:6428–6438

[8] Sanchez-Alarcos V, Recarte V, Perez-Landazabal JI, Gomez-Polo C, Rodriguez-Velamazan JA (2012) Role of magnetism on the martensitic transformation in Ni–Mn-based magnetic shape memory alloys. Acta Mater 60:459–468

[9] Recarte V, Perez-Landazabal JI, Sanchez-Alarcos V, Zablotskii V, Cesari E, Kustov S (2012) Entropy change linked to the martensitic transformation in metamagnetic shape memory alloys. Acta Mater 60:3168–3175

[10] Segui C, Cesari E (2014) Contributions to the transformation entropy change and influencing factors in metamagnetic Ni–Co–Mn–Ga shape memory alloys. Entropy 16:5560–5574. https://doi.org/10.3390/e16105560

[11] Ito W, Ito K, Umetsu RY, Kainuma R, Koyama K, Watanabe K, Fujita A, Oikawa K, Ishida K, Kanomata T (2008) Kinetic arrest of martensitic transformation in the NiCoMnIn metamagnetic shape memory alloy. Appl Phys Lett 92:021908-1–021908-3

[12] Umetsu RY, Ito W, Ito K, Koyama K, Fujita A, Oikawa K, Kanomata T, Kainuma R, Ishida K (2009) Anomaly in entropy change between the parent and martensite phases in the $Ni_{50}Mn_{34}In_{16}$ Heusler alloy. Scr Mater 60:25–28

[13] Segui C, Cesari E (2011) Effect of ageing on the structural and magnetic transformations and the related entropy change in a Ni–Co–Mn–Ga ferromagnetic shape memory alloy. Intermetallics 19:721–725

[14] Perez-Landazabal J, Recarte V, Sanchez-Alarcos V, Gomez-Polo C, Cesari E (2013) Magnetic properties of the martensitic phase in Ni–Mn–In–Co metamagnetic shape memory alloys. Appl Phys Lett 102:101908-1-4

[15] Cong DY, Roth S, Wang YD (2014) Superparamagnetism and superspin glass behaviours in multiferroic NiMn-based magnetic shape memory alloys. Phys Status Solidi B 251:2126–2134

[16] Cong DY, Roth S, Schultz L (2012) Magnetic properties and structural transformations in Ni–Co–Mn–Sn multifunctional alloys. Acta Mater 60:5335–5351

[17] Czaja P, Fitta M, Przewoźnik J, Maziarz W, Morgiel J, Czeppe T, Cesari E (2016) Effect of heat treatment on magnetostructural transformations and exchange bias in Heusler $Ni_{48}Mn_{39.5}Sn_{9.5}Al_3$ ribbons. Acta Mater 103:30–45

[18] Bruno NM, Salas D, Wang S, Roshchin IV, Santamarta R, Arroyave R, Duong T, Chumlyakov YI, Karaman I (2018) On the microstructural origins of martensitic transformation arrest in a NiCoMnIn magnetic shape memory alloy. Acta Mater. 142:1. https://doi.org/10.1016/j.actamat.2017.08.037

[19] Stonaha PJ, Karaman I, Arroyave R, Salas D, Bruno NM, Wang Y, Chisholm MF, Chi S, Abernathy DL, Chumlyakov YI, Manely ME (2018) Glassy phonon heralds as train glass state in a shape memory alloy. Phys Rev Lett 120:245701-1–245701-5

[20] Ito W, Nagasako M, Umetsu RY, Kainuma R, Kanomata T, Ishida K (2008) Atomic ordering and magnetic properties in the $Ni_{45}Co_5Mn_{36.7}In_{13.3}$ metamagnetic shape memory alloy. Appl Phys Lett 93:232503–1–232503-3

[21] Segui C, Cesari E, Lazpita P (2016) Magnetic properties of martensite in metamagnetic Ni–Co–Mn–Ga alloys. J Phys D Appl Phys 49:165007-1–165007-9

[22] Bruno NM, Yegin C, Karaman I, Chen J-H, Ross JH Jr, Liu J, Li J (2014) The effect of heat treatments on $Ni_{43}Mn_{42-}Co_4Sn_{11}$ meta-magnetic shape memory alloys for magnetic refrigeration. Acta Mater 74:66–84

[23] Ito W, Imano Y, Kainuma R, Sutou Y, Oikawa K, Ishida K (2007) Martensitic and magnetic transformation behaviors in Heusler-type NiMnIn and NiCoMnIn metamagnetic shape memory alloys. Met Metall Trans A 38A:759–766. https://doi.org/10.1007/s11661-007-9094-9

[24] Czaja P, Wierzbicka-Miernik A, Rogal L (2018) Segregation and microstructure evolution in chill cast and directionally solidified Ni–Mn–Sn alloys. J Cryst Growth 492:50–59. https://doi.org/10.1016/j.jcrysgro.2018.04.006

[25] Rodriguez-Carvajal J (1993) Recent advances in magnetic structure determination by neutron powder diffraction. Phys B 192(1–2):55–69. https://doi.org/10.1016/0921-4526(93)90108-I

[26] Yan H, Zhang Y, Xu N, Senyshyn A, Brokmeier HG, Esling C, Zhao X, Zuo L (2015) Crystal structure determination of

incommensurate modulated martensite in Ni–Mn–In Heusler alloys. Acta Mater 88:375–388

[27] Marcinkowski MJ, Brown N (1962) Direct observation of antiphase boundaries in the Fe_3Al superlattice. J Appl Phys 33:537–552

[28] Brown PJ, Gandy AP, Ishida K, Kainuma R, Kanomata T, Neumann KU, Oikawa K, Ouladdiaf B, Ziebeck KRA (2006) The magnetic and structural properties of the magnetic shape memory compound $Ni_2Mn_{1.44}Sn_{0.56}$. J Phys Condens Matter 18:2249–2259. https://doi.org/10.1088/0953-8984/18/7/012

[29] Brown PJ, Crangle J, Kanomata T, Matsumoto M, Neumann K-U, Ouladdiaf B, Ziebeck KRA (2002) The crystal structure and phase transitions of the magnetic shape memory compound Ni_2MnGa. J Phys Condens Matter 14:10159–10171. https://doi.org/10.1088/0953-8984/14/43/313

[30] Wang Y, Huang C, Gao J, Yang S, Ding X, Song X, Ren X (2012) Evidence for ferromagnetic strain glass in Ni–Co–Mn–Ga Heusler alloy system. Appl Phys Lett 101:101913-1–101913-4

[31] Santamarta R, Cesari E, Font J, Muntasell J, Pons J, Dutkiewicz J (2006) Effect of atomic order on the martensitic transformation of Ni–Fe–Ga alloys. Scripta Mater 54:1985–1989

[32] Moya X, Manosa L, Planes A, Krenke T, Acet M, Wassermann EF (2006) Martensitic transition and magnetic properties in Ni–Mn–X alloys. Mater Sci Eng A 438–440:911–915

[33] Scarsbrook G, Cook JM, Stobbs WM (1984) The stabilization of martensite in Cu–Zn–Al shape memory alloys. Metall Trans A 15A:1977–1986

[34] Overholser RW, Wuttig M, Neumann DA (1999) Chemical ordering in Ni–Mn–Ga Heusler alloys. Scr Mater 40:1095–1102

[35] Segui C, Pons J, Cesari E (2007) Effect of atomic ordering on the phase transformations in Ni–Mn–Ga shape memory alloys. Acta Mater 55:1649–1655

[36] Marcinkowski MJ, Fisher RM (1963) Theoretical analysis of plastic deformation in superlattices based on the body-centered cubic structure. J Appl Phys 34:2135–2145

[37] Perez-Sierra AM, Bruno NM, Pons J, Cesari E, Karaman I (2016) Atomic order and martensitic transformation entropy change in Ni–Co–Mn–In metamagnetic shape memory alloys. Scr Mater 110:61–64

[38] Chulist R, Czaja P, Tokarski T, Faryna M (2018) Martensite stabilization in single crystalline Ni–Mn–Ga and Ni–Mn–Sn magnetic shape memory alloys. Mater Lett 230:266–269